





# Chapter 1

## Acceleration-Sensitive Interference

### 1.1 Chapter Outline

This chapter describes the aspects of the project aimed at observing matter-wave interference in **rb87!** (**rb87!**) and its subsequent characterisation. The laser system used to drive the necessary Raman transitions is presented in Section 1.2. This is followed by a discussion of the methods used to detect the population in each internal state in Section 1.3. The Raman transition spectrum and dynamics of the atoms during each Raman pulse are discussed in Section ???. This chapter continues with an overview of identified sources of noise and their impact on the interferometer's sensitivity to accelerations in Section 1.5. Finally, a presentation of observed interference and an analysis of its sensitivity to accelerations is given in Section 1.6.

## 1.2 The M-Squared Laser System

This section describes the laser system manufactured by *M-Squared Lasers*, which is used to drive Raman transitions. An overview of the laser system can be found in Section 1.2.1, which includes the techniques used to externally communicate with the laser's ICE-BLOC control modules. The control of the frequency and phase-lock is then described in Section 1.2.2. Finally, this section concludes in Section 1.2.3 with a description of the DCS module which is used to control the amplitude, frequency and phase of the Raman laser beat-note during the experiment.

### 1.2.1 Laser System Overview

The Raman laser system contains two Solstis lasers which generate laser light by pumping a Ti-sapphire crystal housed inside a resonator. The output light is frequency-stabilised using piezo-electric stacks to adjust the resonator length [4]. A schematic diagram of this laser system is given in Figure 1.1. Each laser is seeded using a *Lighthouse Photonics* Sprout laser to generate light around 780 nm. The first laser acts as the master whose frequency is fixed to an absorption feature in the transition spectrum of **rb87!**. The second is slaved to this using a phase-locked loop to keep their beat frequency and relative phase constant. The two beams are mixed on a **pbs!** (**pbs!**), so that they are orthogonally polarised. Two **aom!**s (**aom!**s) control the output power.

The system contains 4 ICE-BLOC modules which implement various types of control. The first two (one for each Solstis) are used to stabilise the output power of each laser by feeding back to the corresponding Sprout laser. They are also used to coarsely adjust the output frequency, which is measured using a *HighFinesse* wavemeter. The third is used for the **pll!** (**pll!**) and feeds-back onto the slave laser to control both the frequency and phase of the optical beat-note between the two lasers. The final

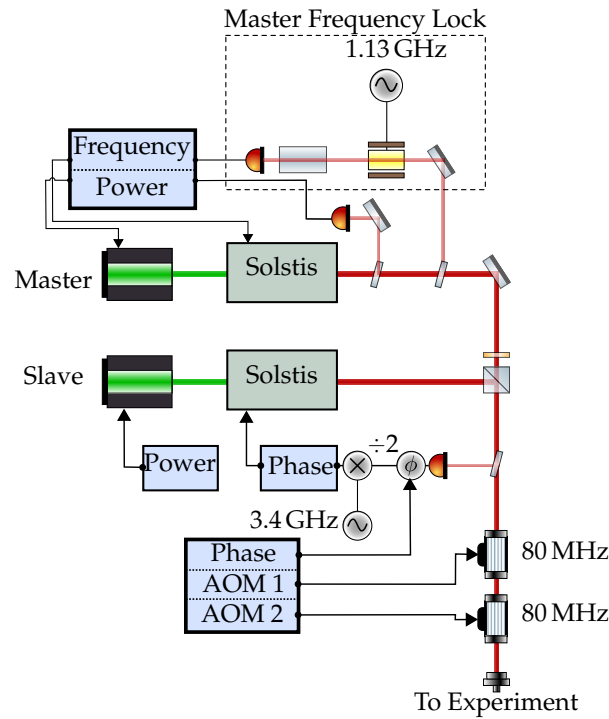


**Figure 1.1:** Schematic Diagram of the M-Squared laser system. Two Solstis lasers provide the two Raman frequencies, which are fibre coupled onto the orthogonal axes of a **pm!** (**pm!**) fibre. Control of the power, frequency and phase as required to drive Raman transitions is handled by the four ICE-BLOC modules indicated in blue. Further detail of this control is given in the text.

ICE-BLOC, referred to as the DCS module, is used to control the lasers in real-time during the experiment.

### External ICE-BLOC Control

The ICE-BLOC modules are able to communicate with each other using an Ethernet hub. Another computer connected to this network is able to control them by accessing a web page that each module hosts. These web pages control the ICE-BLOCs by sending structured JSON messages. This graphical interface can be bypassed by directly communicating these messages. This is done using MOTMaster so that various parameters, such as the frequency and phase of the Raman beat-note, can be automatically varied between each experiment cycle.

## 1.2.2 Frequency and Phase Control

### Master Lock

The frequency of the master laser is stabilised using saturated absorption spectroscopy in a Rubidium vapour cell. Part of the beam is picked off and modulated by an **eom!** (**eom!**). The positive frequency sideband is used to lock the master laser to the 2,3 crossover feature. In effect, this means that the modulation frequency of the **eom!** sets the one-photon detuning of the Raman transition. The modulation frequency is set so that the master laser frequency is 1.13 GHz below the  $|F = 2\rangle \rightarrow |F' = 3\rangle$  transition.

### Frequency and Phase Lock

The optical beat-note between the two lasers is measured using a fast photodiode. The signal from this is used in a **pll!** to fix the relative phase between the two lasers. A frequency divider halves the frequency of the signal before comparing it to a **vco!** (**vco!**) of around 3.4 GHz. This creates an error signal which used to control both the frequency and phase of the beat-note by feeding back to the slave laser Solstis. The relative phase between the two lasers is adjusted using an analogue phase shifter and the frequency difference is controlled by tuning the **vco!** frequency.

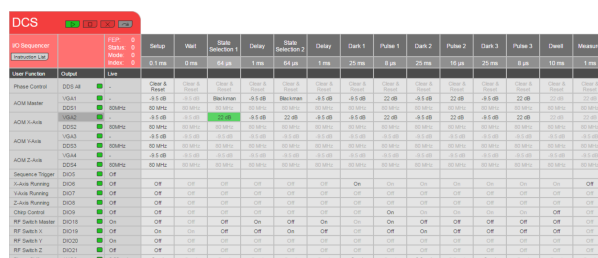
The beat-frequency of the Raman lasers can be chirped by triggering a ramp of the control voltage to the **vco!**. For chirp rates of lower than  $24 \text{ MHz s}^{-1}$ , the phase-lock is able to keep the beat-note phase-coherent during the chirp.

## 1.2.3 The DCS Module

The DCS module is used to control the output of the lasers during the experiment. It uses an on-board **dds!** (**dds!**) to synthesise the 80 MHz driving frequencies for each

This module is used to control the amplitude, frequency and phase of each Raman pulse. The pulse amplitude is shaped using an analogue voltage to control the power of the RF frequency. The voltage output has been calibrated so that the pulse can be shaped to produce a square, Gaussian or Blackman amplitude envelope. A frequency chirp of the beat-note is optionally triggered by sending a digital pulse to the **pll** ICE-BLOC.

The synthesiser can be configured to run continuously, or to wait at a chosen timestep for an external trigger. It can also iterate through a set number of parameters, such as timestep duration or phase shift by re-building the sequence after each cycle.



### 1.3 Atom Detection

This section describes the methods used to measure the number of atoms in each hyperfine ground state and infer the interferometer phase. It begins with a presentation

the optical setup used to collect fluorescent light on a photodiode in Section 1.3.1. The scheme used to detect the atoms by driving  $\sigma^+$  transitions is then described in Section 1.3.1. This concludes with a discussion on converting the measured photodiode signals into atom number and interferometer phase in Section 1.3.3.

### 1.3.1 Optical Setup

A precise measurement of the number of atoms requires that the atom shot noise is the dominant source of uncertainty. The CCD used in previous stages of the experiment is not sensitive enough for this as there is a significant amount of noise in reading out the charge collected at each pixel. Instead, a more sensitive photodiode is used to detect the atoms. With a suitably high bandwidth, the readout time is much faster than the CCD as well, so that the atoms can be detected well before they fall out of the field of view.

A diagram of the setup used to detect the atoms is given in Figure 1.3. It is a triplet system which uses lenses with focal lengths 150 mm, 75 mm and 60 mm in order from the atoms to the photodiode. A ray-tracing simulation of the optical system indicates spherical aberrations on the image. This is caused by the third lens, which was added to shorten the back focal length. The front lens has a diameter of 50.4 mm, so the solid angle subtended by the optics is  $4\pi \times 7.056 \times 10^{-3} \text{sr}$ .

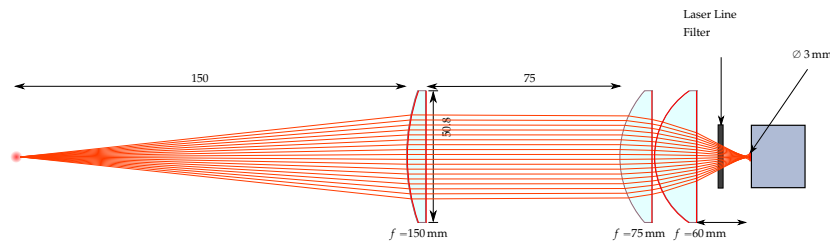


**Figure 1.3:** Optical setup for photodiode detection. A triplet lens system focuses light from radiated from the atoms onto a photodiode. This is mounted using a translation stage to position the photodiode at the back focal point.



## Photodiode Calibration

The photodiode used is a *Femto LCA-S-400K-SI*, which has a trans-impedance amplifier with a bandwidth of 400 kHz and a photo-sensitive area with a diameter of 3 mm. This gives a conversion factor of  $1.84 \times 10^6 \text{ V W}^{-1}$ .

### 1.3.2 Detection using $\sigma^+$ transitions

The atoms are detected using resonance fluorescence from the two vertically aligned **mot!** (**mot!**) beams. A bias field polarises the atoms along the  $\vec{z}$  axis, so the light drives both  $\sigma^+$  and  $\sigma^-$  transitions. The Zeeman shift means that each magnetic sub-level has a different scattering rate, which must be accounted for to calculate the number of atoms. This can be simplified by inverting the handedness of one of the  $\vec{z}$  **mot!** beams using a liquid-crystal **hwp!** (**hwp!**). Now, both beams drive  $\sigma^+$  transitions. The atoms are optically pumped into  $|2, 2\rangle$  and cycle on the  $|2, 2\rangle \rightarrow |3, 3\rangle$  transition. Therefore, only one scattering rate is needed to calculate the number of atoms.

Figure 1.4 shows the setup used to invert the polarisation of one **mot!** beam prior to detection. The liquid-crystal waveplate is an electro-optical device whose birefringence changes when an ac voltage is applied across it. The waveplate is placed at the output of the downward-propagating ( $\vec{z}_-$ ) collimator. The liquid-crystal waveplate is triggered to rotate the incoming linearly polarised light by  $\pi/2\text{rad}$ .

## Detection Sequence

The sequence used to detect the atoms is shown in Figure 1.5. Shortly before the sequence starts, the bias field is aligned to the  $\vec{z}$  axis and the liquid-crystal waveplate is triggered to change the handedness of the  $\vec{z}_-$  beam. The cooling laser frequency

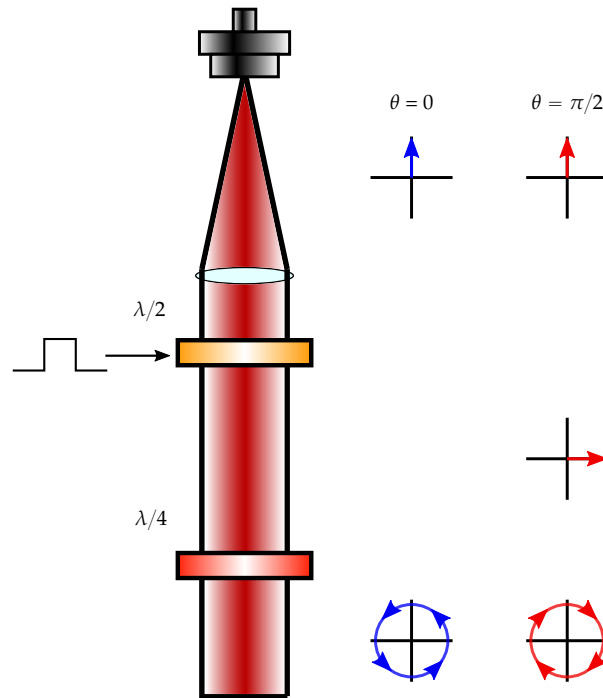


**Figure 1.4:** Scheme to invert beam polarisation. In the **mot!** loading phase of the experiment, the liquid crystal **hwp!** is oriented to give a right-hand circular polarised beam shown in blue. Prior to detection, a digital pulse triggers a re-orientation of its slow axis. This results in a left-hand circular polarised beam, shown in red.

is set so it is detuned by  $\delta_D = 3$  MHz below the  $|F = 2\rangle \rightarrow |F' = 3\rangle$  transition and the repump laser is set to resonance with the  $|F = 1\rangle \rightarrow |F' = 2\rangle$  transition. This creates an optical molasses which avoids heating the atoms so that they remain in the detection volume for a longer period of time. The intensity of the light is reduced to around  $3I_{\text{sat}}$ . As shown below, this intensity was empirically found to minimise the variance in output voltage. The acquisition of the photodiode voltage is triggered to start at the first Dwell time. The cooling light is first switched on, so that only atoms in  $|F = 2\rangle$  scatter light. After this, the repump is switched on, so that atoms in  $|F = 1\rangle$  are optically pumped into  $|F = 2\rangle$  and all the atoms scatter light. This repump light is a sideband of the cooling laser, so the total output is increased to ensure that the intensity of the cooling light remains constant. Each detection step lasts  $250\text{ }\mu\text{s}$ , but the first  $50\text{ }\mu\text{s}$  is discarded to allow time for the intensity to stabilise and for optical pumping into  $|F = 2\rangle$ . The atoms are then blown away by switching off one of the detection beams before the sequence is repeated to collect a background signal.

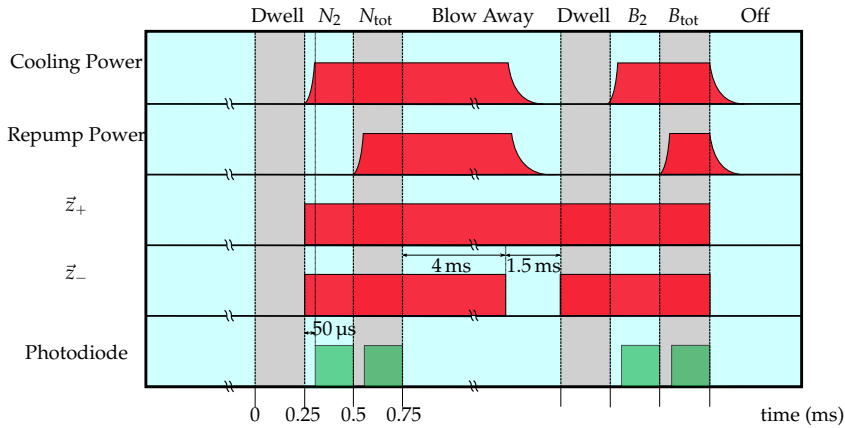


**Figure 1.5:** Timing diagram for state detection. Atoms in  $|F = 2\rangle$  are detected before the repump light pumps those in  $|F = 1\rangle$ , so they are detected as well. A background light measurement for each step is also taken.

### Maximum Detection Time

As the atoms scatter light during detection, the cloud will be heated and expand due to the momentum exchanged from absorption and spontaneous emission. The atoms are only cooled along the axis of the detection beams, so the heating rate is greatest along the other two axes. It is necessary to ensure that the heating rate is low enough that the atoms remain within the detection beam for the entire detection time. A requirement on the maximum detection time can be obtained as follows. The momentum of an atom scattering photons follows a random walk, so the variance of the momentum along one axis after a time  $t$  is  $\langle \Delta p \rangle^2 = 2Dt$ . The scattered photon is equally likely to be emitted in any direction, so the diffusion coefficient is

$$D = \frac{1}{3}(\hbar k)^2 R_{\text{sc}} \quad (1.1)$$

If the cloud has a Gaussian spatial distribution with an initial width of  $\sigma_0$ , the width at a later time of is given by

$$\sigma_x^2(t) = \sigma_0^2 + \frac{2n_p v_r^2 t^2}{3} \quad (1.2)$$

where  $v_r = \frac{\hbar k}{m_{\text{rb}}} = 6 \text{ mm s}^{-1}$  is the recoil velocity and  $n_p$  is the number of photons scattered. To remain within the detection region, the width of the cloud must be smaller than the detection beam waist  $w$ , so the detection time must satisfy

$$t_D \ll \sqrt{\frac{3(w^2 - \sigma_0^2)}{2(nv_r^2)}} \quad (1.3)$$

For a beam waist of 7.5 mm, initial cloud size of 5 mm and a maximum scattering rate of  $2 \times 10^7 \text{ s}^{-1}$  the detection time must be much less than 4.7 ms.

## Optimal Intensity

The optimal intensity was empirically found by varying the total power in the detection beams and recording the photodiode voltage for a fixed detection time of  $200\mu\text{s}$ . Figure 1.6 the average voltage measured by detecting atoms in the  $|F = 2\rangle$  state as the intensity of the light increases. The saturation parameter  $s$  is defined using the peak intensity and by the time they are detected, the atoms have moved from this region. A non-linear least squares fit to the function

$$v = a \frac{bs}{1 + bs + 4(\delta_D/\Gamma)^2} \quad (1.4)$$

gives a scaling for the intensity of  $b = 0.83$ . The variance in the measured voltage (for a constant mean number of atoms) is minimised when the intensity is around  $3I_{\text{sat}}$ . Above this intensity, there is a significant depopulation into  $|F = 1\rangle$  caused by off-resonant excitations to the  $|F' = 2\rangle$  state. This is evident in the voltage signal over time, which is shown in Figure 1.7 for various intensities. At an intensity of  $3I_{\text{sat}}$ , around 5% of the population is pumped out of  $|F = 2\rangle$ .

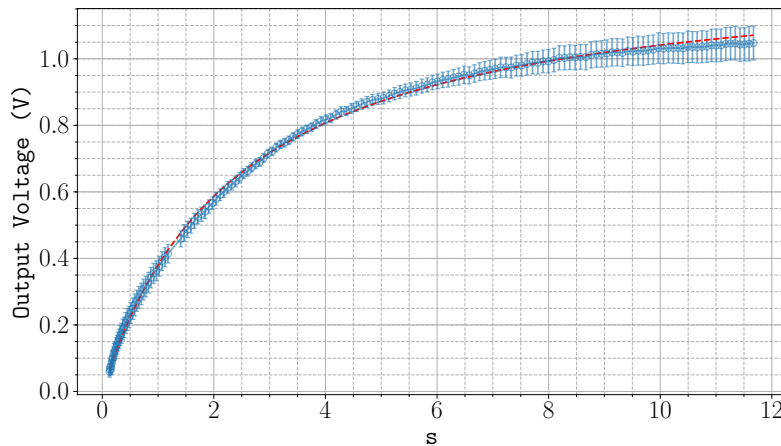


**Figure 1.6:** Photodiode output voltage for increasing detection beam intensity. The red dashed line indicates a fit to equation (1.4) to estimate the scaling factor for the saturation parameter  $s$ .

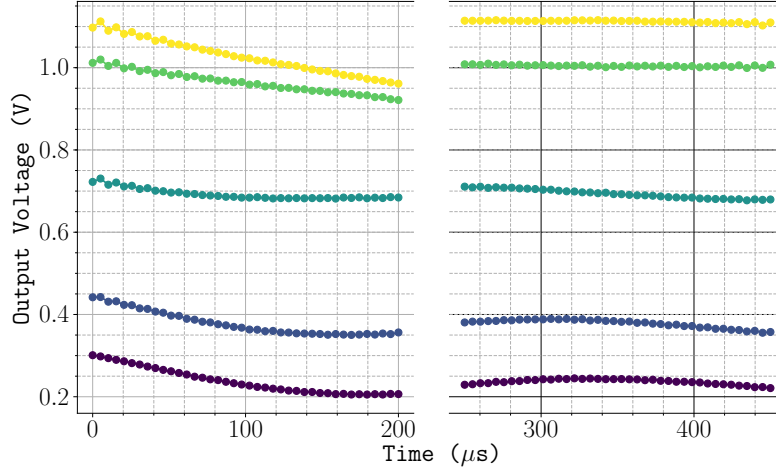


**Figure 1.7:** Photodiode voltage over time during detection for  $s = 0.5, 1, 3, 7, 10$  in order from purple to yellow.

### 1.3.3 Measuring the Occupation Probability

The occupation probability of the  $|F = 2\rangle$  state is obtained by measuring the proportion of atoms in each hyperfine ground state. The number of atoms  $n_{\text{at}}$  that scatter light on the cycling transition is proportional to the photodiode voltage  $U_{\text{pd}}$  as follows

$$\begin{aligned} U_{\text{pd}} &= \eta R_{\text{sc}}(I, \Delta) n_{\text{at}} \hbar \omega G \\ &= \alpha \eta R_{\text{sc}}(I, \Delta) n_{\text{at}} \end{aligned} \quad (1.5)$$

where  $\eta = \Omega/4\pi$  is the fractional solid angle subtended by the collection optics,  $\hbar \omega = 1.6 \text{ eV}$  is the photon energy,  $R_{\text{sc}}$  is the scattering rate defined in equation (??) and  $G$  is the photodiode conversion gain. At the saturation intensity and a detuning of 3 MHz, the voltage measured per atom is around 30 nV per atom. The probability of an atom occupying  $|F = 2\rangle$  is estimated as follows

$$P_{|F=2\rangle} = \frac{N_2 - B_2}{N_{\text{Tot}} - B_{\text{Tot}}} \quad (1.6)$$

where  $N$  and  $B$  denote the average voltage during signal and background measurements, respectively. Subtracting the background signal from each measurement removes the bias that arises from detecting light not scattered by the atoms. The interferometer phase  $\Phi$  is determined from equation (1.6) using

$$P_{|F=2\rangle} = P_0 + \frac{C}{2} \cos(\Phi) \quad (1.7)$$

where  $P_0$  is the mean probability of detecting atoms in  $|F = 2\rangle$  and  $C$  is the interferometer fringe contrast. These are experimentally determined by varying  $\Phi$  as described in Section 1.6.1.

### Atom Number Bias

It is worth describing the voltages measured by the photodiode in more detail. The expression for the population in equation (1.6) assumes that the voltage measured in the  $N_2$  and  $N_{\text{Tot}}$  detection steps are directly proportional to the number of atoms present in  $|F = 2\rangle$  and the total number in the interferometer, respectively. In actual fact, there is a bias in  $N_2$  from the previously mentioned de-population and a bias in  $N_{\text{Tot}}$  from a residual population in the  $|F = 1, m_F = \pm 1\rangle$  states. These contribute to an error in  $P_{|F=2\rangle}$ , which reduces the maximum population that can be detected in  $|F = 2\rangle$ . This causes a reduction in the interferometer fringe contrast and hence, sensitivity. In the following discussion, these systematic errors are addressed emphasise their effect. It is shown that for an increasing fraction of atoms in the  $|1, \pm 1\rangle$  states, this dominates over the depopulation from the  $|F = 2\rangle$  level.

If atoms are pumped out of  $|F = 2\rangle$  at a rate  $\gamma$ , then the number of atoms in the number of atoms in both hyperfine ground states is given by

$$n_2(t) = n_2^i e^{-\gamma t} \quad (1.8)$$

where  $n_2^i$  is the initial number in  $|F = 2\rangle$ . After averaging over a time  $\tau$ , this gives

$$\bar{n}_2 = \frac{n_2^i(1 - e^{-\gamma\tau})}{\gamma\tau} \quad (1.9)$$

Consequently, the number of atoms in  $|F = 1\rangle$  increases. This is expressed as

$$\bar{n}_1 = n_1^i + (1 - e^{-\gamma\tau})n_2^i + n_{\pm 1} \quad (1.10)$$

where  $n_{\pm 1}$  is the background population in  $|1, \pm 1\rangle$ . The bias is the occupation probability is then

$$\delta P = \frac{\bar{n}_2}{\bar{n}_2 + \bar{n}_1} - \frac{n_2^i}{n_1^i + n_2^i} \quad (1.11)$$

This bias has the effect of reducing the interferometer contrast. The residual atoms in  $m_F = \pm 1$  and the depopulation means it is not possible to ever detect the total population in  $|F = 2\rangle$ . The contrast is given by

$$\begin{aligned} C &= P_{\max} - P_{\min} \\ &= 1 - \frac{(1 - e^{-\gamma\tau})}{1 - \alpha} \end{aligned} \quad (1.12)$$

where  $\alpha = \frac{n_{\pm 1}}{n_1 + n_2}$  is the ratio of the number of residual atoms to the number in the interferometer. A plot of the contrast for an increasing proportion of  $m_F = \pm 1$  atoms is shown in Figure 1.8, taking the loss rate of the photodiode signal measured in Figure 1.7



for  $s = 3$ . For an  $m_F = \pm 1$  population of at least 4% of that in  $m_F = 0$ , the reduction in contrast is dominated by the residual atoms.

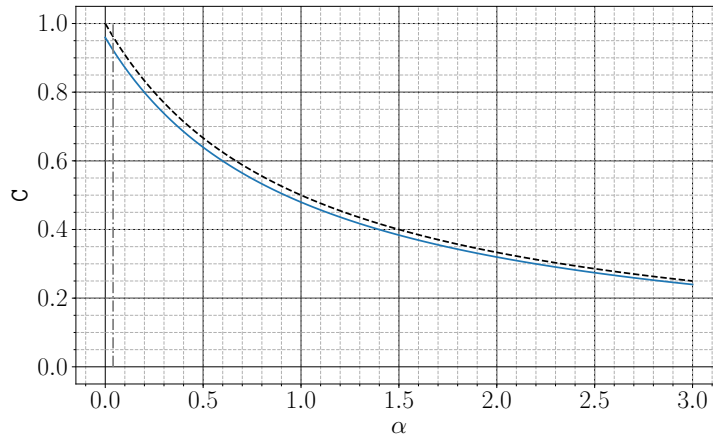


**Figure 1.8:** Interferometer contrast for an increasing residual atom ratio. The black dashed line indicates the reduction expected when no atoms are lost from  $|F = 2\rangle$ . The dot-dashed line indicates the ratio at which the loss in contrast from the residual atom number dominates over the depopulation.

$|F = 2\rangle$  and  $C$  is the interferometer fringe contrast.

## 1.4 Individual Pulse Characterisation

This section presents a characterisation of the pulses used to drive Raman transitions between the two hyperfine ground states. First, the properties of the Raman transition spectrum are presented in Section 1.4.1. Following this, a discussion of cancelling the systematic phase from a differential ac Stark Shift is given in Section 1.4.2. Finally, this section concludes with specific details about the individual pulses used in the experiment. The first Raman pulse, which is used to select a subset of atoms with a narrow velocity spread, is presented in Section 1.4.3. This section concludes with a presentation of the dynamics of the three pulses used to coherently control the atoms during the interferometer in Section 1.4.4

### 1.4.1 Raman Transition Spectrum

The state preparation sequence optically pumps the majority of the atoms into the  $|1,0\rangle$  state. Ideally, each Raman beam is perfectly circularly polarised and can only drive  $|1,0\rangle \leftrightarrow |2,0\rangle$  transitions using either of the counter-propagating pairs of beams. More generally, the selection rules of the Raman transition allow for transitions between other states, depending on the polarisation of the light. The allowed transitions between the different Zeeman states are presented in Table 1.2. The laser polarisation configurations are given in Table 1.1. These are defined for an atom being excited from  $|F = 1\rangle$  and stimulated into  $|F = 2\rangle$ , so that the  $\vec{k}_2$  beam *decreases* the angular momentum when it drives a  $\sigma^+$  transition.

Figure 1.9 shows an example of the Raman transition spectrum. The beat frequency between the two Raman lasers is scanned and the light is pulsed for 160  $\mu\text{s}$  to drive atoms into the  $|F = 2\rangle$  state. There is a large peak close to the hyperfine splitting frequency. This peak is a result of Doppler-insensitive co-propagating transitions<sup>1</sup>. This indicates that the two Raman beams are not orthogonally circularly polarised, as that cannot drive co-propagating transitions. This is further supported by the fact that there are  $\Delta m = \pm 1$  transitions, which can only occur if one of the lasers drives a  $\pi$  transition. The Zeeman shift on the co-propagating transitions between  $|F = 1,0\rangle \rightarrow |F = 2,1\rangle$  and  $|F = 1,1\rangle \rightarrow |F = 2,1\rangle$  are 95 kHz and 189.5 kHz, which correspond to a bias field of 1.35 G.

Each co-propagating transition from  $|1,0\rangle$  has two smaller peaks which are the Doppler-sensitive counter-propagating transitions. The central peak is shown in more detail in Figure 1.10. The counter-propagating transitions are shifted by  $-185$  kHz and  $+215$  kHz respectively, which correspond to velocities of  $7.2 \text{ cm s}^{-1}$  and  $8.4 \text{ cm s}^{-1}$ . The

<sup>1</sup>When the two light fields are co-propagating, the Doppler resonance term  $\delta_D \propto \vec{k}_1 - \vec{k}_2$  is close to zero

		$\vec{k}_2$		
		$\sigma^-$	$\pi$	$\sigma^+$
$\vec{k}_1$	$\sigma^-$	c <sub>1</sub>	c <sub>2</sub>	–
	$\pi$	c <sub>3</sub>	–	c <sub>4</sub>
	$\sigma^+$	–	c <sub>5</sub>	c <sub>6</sub>

**Table 1.1:** Labels for Raman transitions excited from  $|F = 1\rangle$  by  $\vec{k}_1$  and stimulated into  $|F = 2\rangle$  by  $\vec{k}_2$ .

		$ F = 2, m\rangle$				
		-2	-1	0	1	2
$ F = 1, m\rangle$	-1	(c <sub>2</sub> , c <sub>4</sub> )	(c <sub>1</sub> , c <sub>6</sub> )	(c <sub>3</sub> , c <sub>6</sub> )	–	–
	0	–	(c <sub>2</sub> , c <sub>4</sub> )	(c <sub>1</sub> , c <sub>6</sub> )	(c <sub>3</sub> , c <sub>6</sub> )	–
	1	–	–	(c <sub>2</sub> , c <sub>4</sub> )	(c <sub>1</sub> , c <sub>6</sub> )	(c <sub>3</sub> , c <sub>6</sub> )

**Table 1.2:** Allowed polarisation configurations between each hyperfine ground state Zeeman sub-levels.

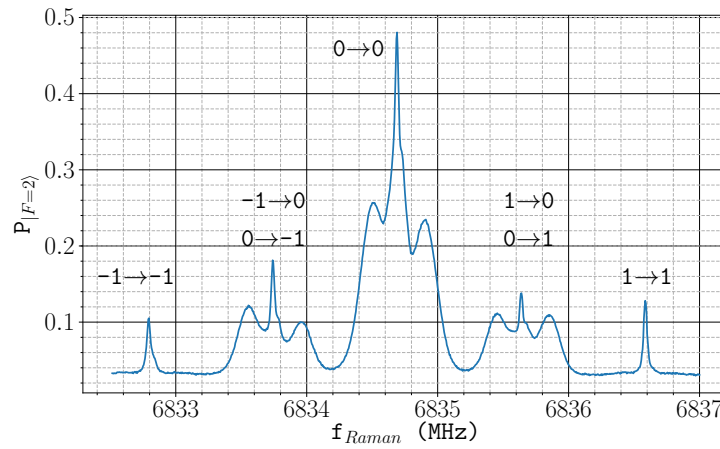


**Figure 1.9:** Raman transition spectrum, obtained by scanning the beat frequency of the two Raman lasers. The transitions  $|1, m_F\rangle \rightarrow |2, m'_F\rangle$  are indicated at each observed peak.

same Doppler shifts are also observed in the peaks corresponding to the  $|F = 1, m_F = 0\rangle \rightarrow |F = 2, m_F = \pm 1\rangle$  transitions. The counter-propagating transitions are Doppler-broadened by the thermal velocity of the atoms along the direction of the Raman beams. Fitting the transition to the lineshape expected from a thermal distribution of atoms gives a temperature of 15  $\mu\text{K}$  and 13.5  $\mu\text{K}$  from each counter-propagating transition. At the time this spectrum was measured, the molasses was not optimised to give the lowest temperature.

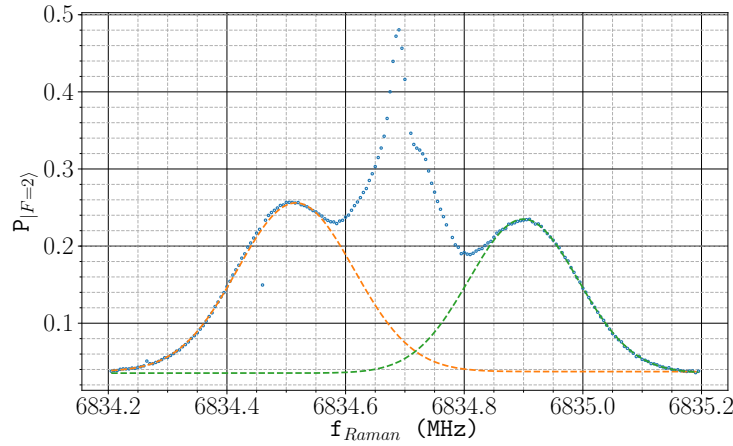


**Figure 1.10:** Transition spectrum showing the  $\Delta m = 0$  transition from  $|1, 0\rangle$ . The orange and green dashed lines are fits to a Doppler-broadened lineshape for each of the counter-propagating profiles.

### 1.4.2 Cancelling the Differential ac Stark Shift

It is worth considering the effects of ac Stark shifts on the atom interferometer. Firstly, they are intrinsically related to the effective Rabi frequency and as such, cannot be avoided. The average ac Stark shift  $\Omega_{\text{avg}}^{\text{ac}} = (\Omega_1^{\text{ac}} + \Omega_2^{\text{ac}})/2$  (see Section ?? for more details) is the same along both paths of the interferometer, provided that the intensity variation of the Raman beams over the path separation can be neglected. Therefore, this should not lead to an observable phase shift.

On the other hand, the differential ac Stark shift  $\delta^{\text{ac}} = \Omega_1^{\text{ac}} - \Omega_2^{\text{ac}}$  can lead to an observable phase shift. Using the results from Ref. [10] for  $\pi$  and  $\frac{\pi}{2}$  pulses, the phase shift to a Mach-Zender type interferometer is

$$\Delta\Phi^{\text{ac}} = \frac{\delta_3^{\text{ac}}}{\Omega_{\text{eff}}} - \frac{\delta_1^{\text{ac}}}{\Omega_{\text{eff}}} \quad (1.13)$$

where  $\delta_3^{\text{ac}}$  and  $\delta_1^{\text{ac}}$  are the ac Stark shifts of the last and first  $\frac{\pi}{2}$  pulses, respectively. Therefore, the interferometer is sensitive to the difference in the ac Stark shift of these pulses.

As the atoms fall under gravity, it is likely that the intensity of the Raman beams during these pulses will not be the same. Fortunately, it is possible to eliminate this differential phase shift using an appropriate choice of intensity and detuning of the Raman lasers. This can be seen by first writing out the differential ac Stark shift

$$\delta^{\text{ac}} = \Omega_1^{\text{ac}} - \Omega_2^{\text{ac}} = \sum_k \frac{|\Omega_{1k}|^2}{4\Delta_{1k}} - \sum_k \frac{|\Omega_{2k}|^2}{4\Delta_{2k}} \quad (1.14)$$

in terms of the one-photon Rabi frequencies  $\Omega_{ik}$  and detunings  $\Delta_{ik}$ . When both Raman beams are red-detuned from all the one-photon transitions, both terms in equation (1.14) are strictly negative. Therefore,  $\delta^{\text{ac}}$  can be cancelled by choosing the correct intensities for each Raman beam. A plot of  $\delta^{\text{ac}}$  for various Raman beam intensities as a function of the ratio between the two Raman beams is shown in Figure 1.11a. There is a ratio at which the differential ac Stark shift cancels and is independent of the total intensity. The ratio that cancels  $\delta^{\text{ac}}$  for increasing two-photon detuning  $\Delta_R$  is shown in Figure 1.11b. When  $\Delta_R$  is 1.13 GHz below the  $|F = 2\rangle \rightarrow |F' = 3\rangle$  transition, this ratio is maximised. The differential ac Stark shift is cancelled when the intensity ratio of light driving  $|1, 0\rangle$  transitions to  $|2, 0\rangle$  transitions is  $\mathcal{R} = 0.583$ .

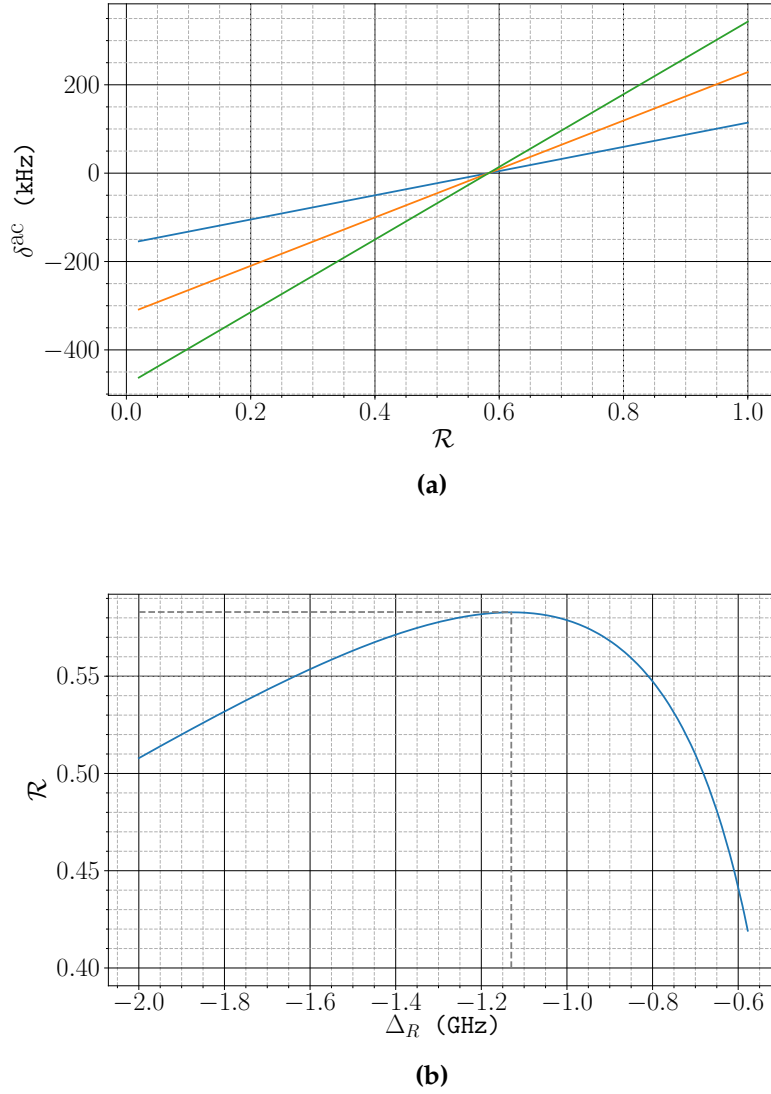


**Figure 1.11:** The effects of the Raman beam intensities and detuning on the differential ac Stark shift  $\delta^{\text{ac}}$ . **(a)** shows  $\delta^{\text{ac}}$  as a function of the intensity ratio  $\mathcal{R}$  between the light which drives transitions from  $|1, 0\rangle$  to the light that couples to  $|2, 0\rangle$  for the two-photon detuning of  $\Delta_R = -1.13 \text{ GHz}$  used in the experiment. Example intensities for the  $|2, 0\rangle$  light are  $100 \text{ W m}^{-2}$  (blue),  $200 \text{ W m}^{-2}$  (orange) and  $300 \text{ W m}^{-2}$  (green). **(b)** shows how the ratio for which  $\delta^{\text{ac}} = 0$  varies as  $\Delta_R$  increases. The dashed lines indicate the value of  $\Delta_R$  used in the experiment and its corresponding ratio of 0.583.

Since it is not straight-forward to directly measure the intensity of each Raman beam on the atoms, a better method to cancel the differential ac Stark shift is to use the transition spectrum to determine when the intensity of the lasers are set to the appropriate ratio. Experimentally, this was done by adjusting the power of the pump lasers for the master and slave Solstis lasers. When the master is seeded with 10 W and the slave with 6.5 W, the differential ac Stark shift is eliminated. Figure 1.12 shows the transition spectrum using two different effective Rabi frequencies, corresponding to  $\pi$  pulse times of 22.5  $\mu\text{s}$  and 45  $\mu\text{s}$ . In this instance, the frequency difference of the two co-propagating peaks is less than 1 kHz. There is also a shift of 1.4 MHz from  $f_{\text{hfs}}$ . This is

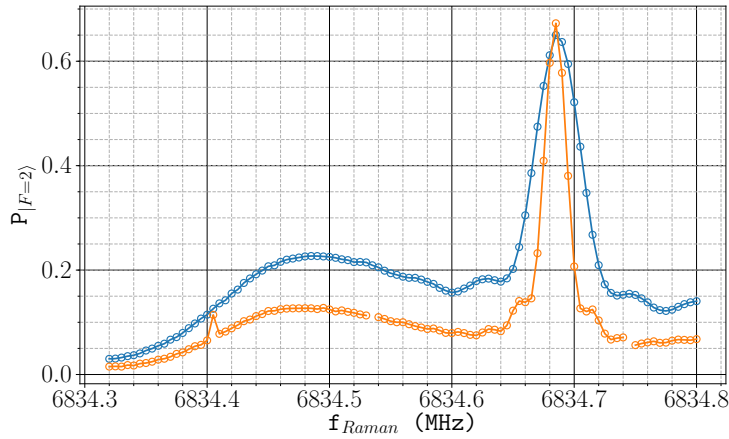


**Figure 1.12:** Raman transition spectrum after cancelling the differential ac Stark shift. The blue (orange) curve shows a pulse with a  $\pi$  pulse time of 22.5  $\mu\text{s}$  (45  $\mu\text{s}$ ).

a result of a second-order Zeeman shift and corresponds to a field strength of 1.56 G.

### 1.4.3 Velocity-Selective Pulse

The Raman transition is Doppler-sensitive, so the velocity spread of atoms contributes to their dynamics. At a temperature of 6  $\mu\text{K}$ , the Doppler width is  $\sigma_f = \frac{2}{\lambda} \sqrt{\frac{k_b T}{m}} \approx 60 \text{ kHz}$ . Coherent control of the atomic state during the interferometer requires that the linewidth of the Raman transition must be much broader than the Doppler width. This

ensures that each atom is driven at approximately the same Rabi frequency, reducing the dephasing rate of the atomic coherence. The linewidth of a Raman transition is determined solely by the pulse intensity and duration. A pulse duration of 7  $\mu\text{s}$  has a linewidth close to the Doppler width, but the intensities required for this are above what is attainable with our Raman laser.

It is possible to reduce the Doppler width of the participating atoms by first applying a Raman pulse to select a subset of the population with a narrower velocity spread [7]. This velocity-selective pulse has a narrower linewidth than the subsequent interferometer pulses. This ensures that the Doppler width of atoms in the interferometer is small compared with the Raman transition linewidth.

Starting with a velocity distribution of atoms described by a 1-D Maxwell-Boltzmann distribution all occupying the  $|1,0\rangle$  state, the population in  $|2,0\rangle$  after applying a Raman pulse is distributed according to

$$P_{|2,0\rangle}(v) = \frac{\Omega_{\text{eff}}^2}{\Omega_{\text{eff}}^2 + \delta^2} \sin\left(\sqrt{\Omega_{\text{eff}}^2 + \delta^2} \tau\right)^2 p(v) \quad (1.15)$$

where  $\delta$  is the Raman detuning defined in equation (??),  $p(v) = \sqrt{\frac{m}{2\pi k_B T}} e^{-\frac{mv^2}{2k_B T}}$  is the velocity distribution and  $\Omega_{\text{eff}}$  is the effective Rabi frequency defined in equation (??). Figure 1.13 shows a simulation of the distribution of atoms driven by a  $\pi$  pulse with a duration of 40  $\mu\text{s}$  and a temperature of 6  $\mu\text{K}$ . The population that is stimulated has a mean velocity shifted by twice the recoil velocity. In this instance, the rms frequency is  $\sigma_f = 19.7 \text{ kHz}$ .

### Velocity-Selected Distribution

The velocity distribution of atoms after the velocity selective pulse can be measured using a second Raman pulse as a probe. In contrast to the interferometer pulses, this



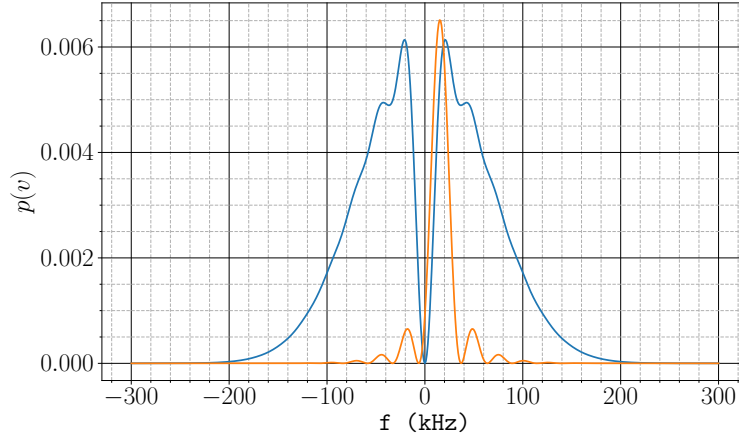


**Figure 1.13:** Velocity distribution of a 6  $\mu\text{K}$  ensemble of atoms after a 40  $\mu\text{s}$  Raman  $\pi$  pulse. The mean velocity of the stimulated distribution, shown in orange, is increased due to the recoil during the transition.

probe must be much lower power than the velocity-selective pulse so that its linewidth is comparatively narrow. A measurement of the velocity distribution of the atoms is shown in Figure 1.14. An initial 40  $\mu\text{s}$   $\pi$  pulse with a Raman beat frequency  $f_v = 6834.51$  MHz prepares atoms in  $|1, 0\rangle$ , before blowing away the atoms which remain in  $|F = 2\rangle$ . After 10 ms, a 80  $\mu\text{s}$   $\pi$  pulse transfers some of the remaining population back into  $|2, 0\rangle$ . The frequency of the probe pulse is varied by chirping the Raman laser beat frequency. In this instance, the power of the pulse was not tuned to give a  $\pi$  pulse area so the measured population is not indicative of the maximum driven by the Raman transition. It is clear that the velocity distribution of the selected atoms is narrower than the initial thermal distribution. Fitting to a 1D Maxwell-Boltzmann distribution gives an effective temperature of around 1  $\mu\text{K}$ .

#### 1.4.4 Interferometer Pulses

The atoms are coherently controlled by pulsing the Raman light to drive Rabi oscillations between the two  $m_F = 0$  hyperfine ground states. The appropriate pulses areas

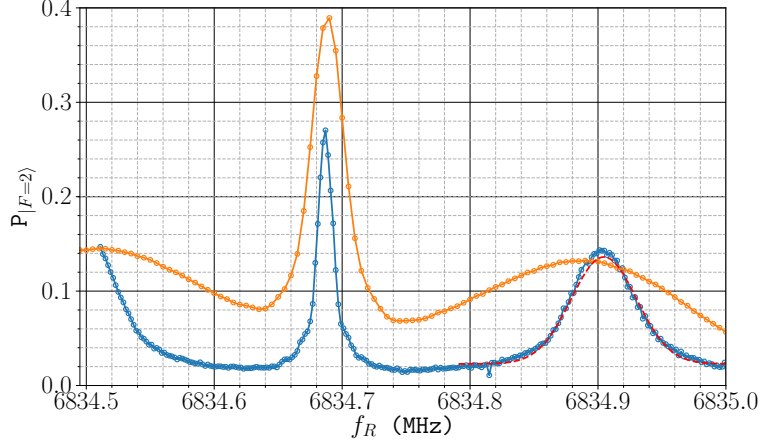


**Figure 1.14:**  $|F = 2\rangle$  population after a Raman pulse at a frequency  $f_v = 6834.51$  MHz transfers atoms to  $|1, 0\rangle$ . This distribution is probed by applying a narrow pulse at a frequency  $f_R$ . The population measured in  $|F = 2\rangle$  is shown in blue. The red dashed line is a fit to a 1D Maxwell-Boltzmann distribution of the Doppler-broadened transition peak. For comparison, the transition spectrum of a single  $\tau = 40 \mu\text{s}$   $\pi$  pulse is shown in orange.

were empirically determined by observing Rabi oscillations at the corresponding time for each interferometer pulse. These are shown in Figure ?? . The power in each Raman laser was set so that a  $\pi$  pulse was achieved with a pulse duration of  $\tau = 15 \mu\text{s}$ . It is clear that the oscillations are rapidly damped. Furthermore, this dephasing rate depends on the time at which the pulse is applied. Since the atoms are at different positions in the beam, this suggests that the dephasing is caused by a spatial variation of the Rabi frequency. This is largely a result of irregularities in the Raman beam wavefront from defects in the aspheric lenses. The Gaussian intensity distribution of each beam is unlikely to cause such a fast dephasing, since the atoms remain close to the centre of the beams.

## 1.5 Sensitivity

This section presents a discussion of some of the major sources of noise in the interferometer.

### 1.5.1 The Allan Variance

For the purposes of this experiment, the sensitivity of the interferometer relates to the minimum value of uncertainty that can be placed on a measurement of acceleration. As such, the limit to the sensitivity is given by the measurement noise. One possible way to characterise this is to use the variance. However with a finite sequence of measurements, this depends on the number of samples and might not converge as the number of samples increases. On the other hand, the two-sample variance

$$\sigma_a^2(2, \tau) = \frac{1}{2} \left\langle (a_{n+1} - a_n)^2 \right\rangle \quad (1.16)$$

does not depend on the number of samples. This can be generalized to longer time separations  $t = N\tau$  by taking the mean of  $N$  consecutive measurements

$$\sigma_a^2(2, t) = \frac{1}{2} \left\langle \left( \frac{1}{N} \sum_{k=0}^{N-1} a_{n+1} - \frac{1}{N} \sum_{k=N}^{2N-1} a_n \right)^2 \right\rangle \quad (1.17)$$

which is referred to as the Allan variance [1]. If the noise in each measurement is uncorrelated, then this becomes

$$\sigma_a(2, t) = \frac{1}{\sqrt{N}} \sigma_a(2, \tau) \quad (1.18)$$

The variance is also related to the signal-to-noise ratio of the observed interferometer fringes. From the interferometer signal defined in equation (1.7), the variance at the

mid-point of the fringe  $\Delta\phi = \pi/2$  is given by

$$\sigma_P^2 = \sigma_{P_0}^2 + \frac{C^2}{4} \sigma_{\Delta\phi}^2 \quad (1.19)$$

The signal-to-noise ratio

$$\left( \frac{S}{N} \right) = \frac{C}{2\sigma_P} \quad (1.20)$$

is the ratio of the fringe amplitude to the standard deviation of the interferometer signal. Under the assumption that  $P_0$  and  $C$  do not fluctuate, the signal-to-noise ratio is related to the interferometer phase and acceleration uncertainties by

$$\left( \frac{S}{N} \right)^{-1} = \sigma_{\Delta\phi} = \mathbf{k}_{\text{eff}} T^2 \sigma_a \quad (1.21)$$

### 1.5.2 Sources of Noise

Some potential sources of noise have been investigated to determine their magnitude. These are not a complete list of the effects which reduce the sensitivity to accelerations, but are the most dominant. The identified sources and their estimated effects on acceleration measurements are shown in Table 1.3. The largest contributor comes from vibrations of the retro-reflecting mirror. Other noise sources, such as magnetic field gradients, laser intensity noise and rotations have not yet been characterised.

### 1.5.3 Detection Noise

Each measurement of the number of atoms has an uncertainty due to random processes that influence the voltage measured by the detector. These errors combine to

Noise Source	Signal/Noise	$\sigma_a$ ( $\mu\text{m s}^{-2}$ )
Atom shot noise ( $5 \times 10^6$ atoms)	2200	0.07
Laser phase noise	157	1
Detection noise	15	10.5
Vibrations	5.8	26

**Table 1.3:** Comparison of known noise sources and their effects on acceleration measurements. These values are estimated assuming a separation between pulses of  $T = 25$  ms and a  $\pi/2$  pulse time of  $\tau = 20$   $\mu\text{s}$ .

give an uncertainty in the interferometer phase and hence, acceleration. It is worth distinguishing between the different sources of noise in measuring the number of atoms. Uncertainties due to fluctuations in the number of atoms and detected photons per measurement cannot be reduced below their shot-noise levels. In particular, the phase noise corresponding to the atom shot noise is the minimum value attainable. Therefore, it is essential that the photo-detector used is sensitive enough to ensure that this does not limit the sensitivity [9].

### Atom and Photon Shot Noise

The discrete nature and the fact that atoms are loaded into the experiment and scatter photons at a constant rate mean that the statistics on the number of atoms and photons are well-described by Poisson distributions. It follows that the number of atoms in the interferometer as well as the number of photons arriving at the detector during each measurement have shot noise fluctuations. From equation (1.5), these are related to an equivalent output voltage as follows

$$\sigma_{\text{at},v}^2 = \alpha^2 \eta^2 R_{\text{sc}}^2 n_{\text{at}} \quad (1.22)$$

$$\sigma_{\text{p},v}^2 = \alpha^2 \eta R_{\text{sc}} n_{\text{at}} \quad (1.23)$$

where  $\sigma_{at,v}$  dominates, provided at least one photon per atom is detected. Hereafter, no attention will be paid to the photon shot noise. For the detection parameters previously defined, the shot noise is equal to around 46.5 nV per atom.

In order for the uncertainty in the atom number to be dominated by the atom shot noise, the detector must be sensitive enough that it has a **nep!** (**nep!**) much lower than the noise in the optical power detected. The **nep!** of a detector is defined as the equivalent optical power which gives a signal-to-noise ratio of 0 after an integration time of 0.5 s. It is convenient to express this as a voltage density, by multiplying it by the photodiode gain. Hence, the voltage density of a detector whose sensitivity is at the atom shot noise level for an integration time  $\tau_D$  is given by

$$V_{at} = \frac{\sigma_{at,v}}{\sqrt{1/2\tau_D}} \quad (1.24)$$

.

### Photodiode Technical Noise

Technical noise in the detector typically arises from multiple electronic processes – such as Johnson noise and shot noise in the current – but it is not necessary to consider them independently in the following discussion. The technical noise of the detector can be estimated by measuring the output voltage when no light is collected. A plot of the power spectral density of the photodiode is shown in Figure ?? taken with a sampling frequency of 200 kHz. The photodiode was covered and the output voltage was sampled for 2 s. The power spectral density has been calculated using Welch's method [11]. The data are partitioned before calculating the Fourier transform of each subset and taking the average. This has the effect of reducing the variance in the estimated power spectrum at the expense of reducing the frequency resolution.

Below 10 kHz the power spectral density is close to uniform with a value of around  $5 \times 10^{-13} \text{ V}^2 \text{ Hz}^{-1}$ , which corresponds to a noise-equivalent power of  $391 \text{ fW Hz}^{-1/2}$ . For higher frequencies, the power spectral density starts to increase. The plot also indicates the corresponding voltage noise density to reach the atom shot noise limit for atom numbers of  $n_{\text{at}} = 5 \times 10^6$  and  $1 \times 10^6$  with the previously defined output voltage per atom. Averaging the detection signal over a time  $\tau$  has the effect of

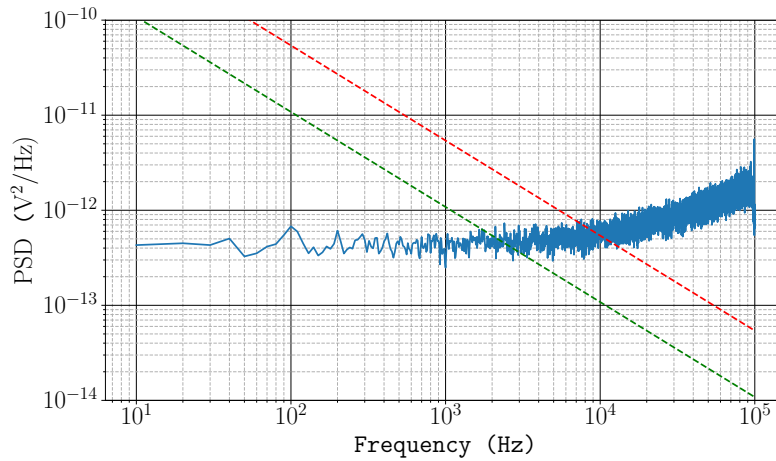


**Figure 1.15:** Power spectral density of the photodiode output voltage sampled for 2 s at a rate of 200 kHz. The red and green dashed lines indicate the required voltage noise density to equal the atom shot noise level after integrating for  $\tau = 2/f_s$  for atom numbers of  $5 \times 10^6$  and  $1 \times 10^6$ , respectively.

filtering the signal above the Nyquist frequency  $f_n = 1/(2\tau)$ . The variance in the averaged voltage over successive shots i.e. the Allan variance, is related to the power spectral density as follows

$$\sigma_{\text{av}}^2(\tau) = 2 \int_0^\infty \frac{\sin(\pi\tau f)^4}{(\pi\tau f)^2} S(f) \, df \quad (1.25)$$

Using equation (1.25), it is possible to determine the detection time required to reduce the shot-to-shot variance below the atom shot noise level. A plot of the Allan deviation for increasing integration time is shown in Figure ??, along with the rms voltage expected for the same numbers of atoms used in Figure 1.15. At the integration time of

200  $\mu\text{s}$ , the detector noise is close to 5  $\mu\text{V}$  – well below the level of the atom shot noise.

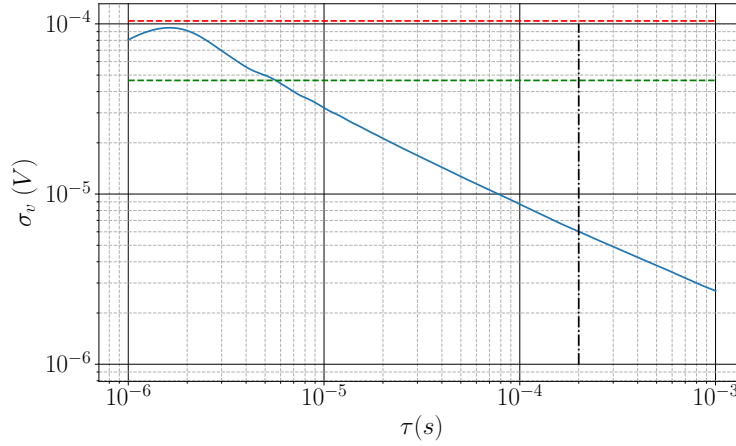


**Figure 1.16:** Allan variance of the Photodiode voltage for increasing integration time  $\tau$ . The red and green dashed lines are the atom shot noise rms voltages for the values used in Figure 1.15. The black dot-dashed line indicates the integration time of 200  $\mu\text{s}$  used in the experiment.

### 1.5.4 The Sensitivity Function

The sources of noise presented thus far arise from statistical uncertainties in measuring the number of atoms and are not present in the ideal case of perfect interferometer contrast. However, there are still other sources which introduce interferometer phase noise. Generally speaking, these add a random component to the interferometer phase which is independent of the forces acting on the atoms. Two dominant sources of phase noise are vibrations of the retro-reflecting mirror and laser phase noise, i.e. fluctuations in the relative phase between the two Raman light fields.



The sensitivity function [3] defines the instantaneous shift of the interferometer phase  $\delta\Phi$  at a time  $t$  due to a phase shift of the Raman laser phase  $\delta\phi$

$$g(t) = \lim_{\delta\phi \rightarrow 0} \frac{\delta\Phi(\delta\phi, t)}{\delta\phi} \quad (1.26)$$

so the interferometer phase shift induced by fluctuations of  $\phi$  is given by

$$\begin{aligned} \Phi &= \int_{-\infty}^{\infty} g(t) \delta\phi \, d\phi(t) \\ &= \int_{-\infty}^{\infty} g(t) \frac{d\phi}{dt} dt \end{aligned} \quad (1.27)$$

In the case of a  $\pi/2 - \pi - \pi/2$  interferometer pulse sequence of durations  $\tau_R - 2\tau_R - \tau_R$  and where  $t = 0$  is defined at the centre of the  $\pi$  pulse, the sensitivity function is

$$g(t) = \begin{cases} \sin(\Omega t) & 0 < t < \tau_R \\ 1 & \tau_R < t < \tau_R + T \\ \sin(\Omega(t - T)) & \tau_R + T < t < 2\tau_R + T \end{cases} \quad (1.28)$$

for a pulse separation time  $T$ .

### 1.5.5 Influence of Laser Phase Noise

The response of the interferometer phase to laser phase noise is best understood in the frequency domain. In particular, the inverse of the interferometer pulse separation time The effects of  $\phi$  are best thought of in terms of its Fourier components. Writing  $\phi(t) = A \cos(\omega t + \psi)$ , equation (1.27) becomes

$$\Phi = -A\omega \cos(\psi) \int_{-\infty}^{\infty} g(t) \sin(\omega t) dt \quad (1.29)$$

where the term proportional to  $\cos(\omega t)$  has been dropped, since  $g(t)$  is an odd function. The integrand in equation (1.29) is proportional to the Fourier transform of  $g(t)$

$$G(\omega) = -i \int_{-\infty}^{\infty} g(t) \sin(\omega t) dt \quad (1.30)$$

which using equation (1.28) becomes [2]

$$G(\omega) = \frac{4i\Omega}{\omega^2 - \Omega^2} \sin\left(\frac{\omega(T + 2\tau)}{2}\right) \left( \cos\left(\frac{\omega(T + 2\tau)}{2}\right) + \frac{\omega T}{2} \sin\left(\frac{\omega T}{2}\right) \right) \quad (1.31)$$

so equation (1.27) becomes

$$\begin{aligned} \Phi &= -iA \cos(\psi) \omega G(\omega) \\ &= -A \cos(\psi) |H(\omega)| \end{aligned} \quad (1.32)$$

A plot of the transfer function  $|H(\omega)|^2$  is presented in Figure 1.17 for  $T = 20$  ms and  $\tau = 20$   $\mu$ s. The asymptotic properties of the transfer function can be summarised as follows:

- At low frequencies  $\omega \ll \Omega$ , the transfer function is approximated by

$$|H(\omega)|^2 \approx 16 \sin^4\left(\frac{\omega T}{2}\right) \quad (1.33)$$

which is a periodic function that is zero at frequency multiples of  $1/\pi T$

- At frequencies  $\omega \gg \Omega$ , the transfer function is

$$|H(\omega)|^2 \approx 4 \frac{\Omega^2}{\omega^2} \sin^2(\omega T) \quad (1.34)$$

which is zero at multiples of  $1/2\pi T$  and is a low-pass first-order filter.

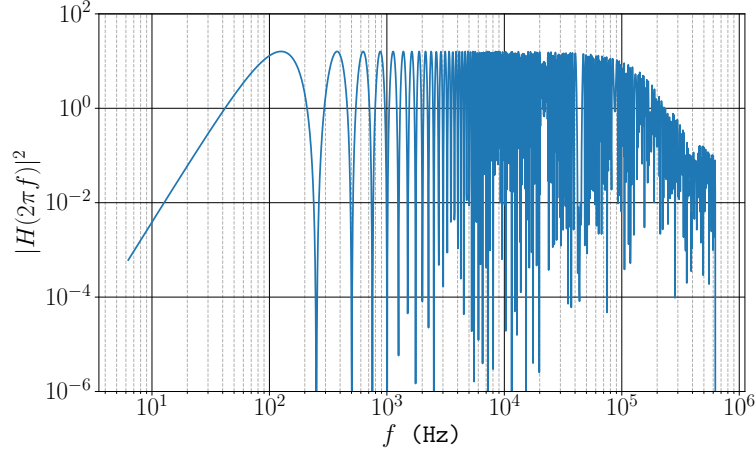


**Figure 1.17:** Transfer function for laser phase noise. Here, the separation between pulses is  $T = 20$  ms and the  $\pi/2$  pulse time is  $\tau = 20$   $\mu$ s.

The variance of  $\Phi$  is obtained by averaging over  $\psi$

$$\sigma_{\Phi}^2 = \langle \Phi^2 \rangle_{\psi} = \frac{1}{2} A^2 |H(\omega)|^2 \quad (1.35)$$

which is related to the phase noise power spectral density  $S_{\phi}(\omega)$  by

$$\sigma_{\Phi}^2 = \frac{1}{2} \int_{-\infty}^{\infty} S_{\Phi}(\omega) |H(\omega)|^2 \frac{d\omega}{2\pi} = \int_0^{\infty} S_{\Phi}(\omega) |H(\omega)|^2 \frac{d\omega}{2\pi} \quad (1.36)$$

Similarly, the Allan variance can be expressed using the transfer function and the phase noise power spectral density [5]. The integration time  $\tau_{\text{av}} = mT_c$  is expressed in multiples of the experiment cycling time  $T_c$ . In the frequency domain, the phase noise power spectral density is sampled at frequency multiples of  $f_c = 1/T_c$ , so the Allan variance becomes

$$\sigma_{\Phi}^2(\tau_{\text{av}}) = \frac{1}{\tau_{\text{av}}} \sum_{k=1}^{\infty} |H(2\pi k f_c)|^2 S_{\phi}(2\pi k f_c) \quad (1.37)$$

The laser phase noise originates from the reference oscillator used in the phase-locked loop for the M-Squared laser. The phase noise spectral density and corresponding Allan deviation for increasing integration time was measured by M-Squared during installation of the laser system. A plot of the Allan deviation is shown in Figure ?? . At an interferometer pulse separation of  $T = 25$  ms, the phase noise in the Raman laser results in an uncertainty in the interferometer phase of 10 mrad.

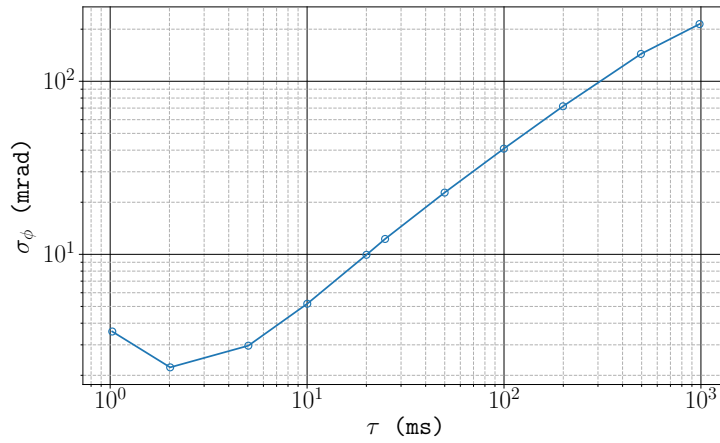


**Figure 1.18:** Allan deviation of the Raman laser phase difference for increasing integration time. Data reproduced from [M2\_manual].

### 1.5.6 Vibrations

The phase difference between the two Raman beams depends on the position of the retro-reflecting mirror. Consequently, this defines a frame of reference for the position of the atoms during the interferometer. Any random motion of the mirror, for instance from mechanical vibrations, introduces a random component to the laser phase. An acceleration of the mirror modifies the laser phase as follows

$$\frac{d^2\Phi(t)}{dt^2} = \mathbf{k}_{\text{eff}} \cdot \mathbf{a}(t) \quad (1.38)$$

and the sensitivity to accelerations  $g_a$  is given by

$$\frac{1}{k_{\text{eff}}} \frac{d^2 g_a(t)}{dt^2} = g(t) \quad (1.39)$$

$$(1.40)$$

Assuming that the pulse time  $\tau$  is much shorter than the interferometer pulse separation,  $T$ , the acceleration sensitivity function is approximated by

$$g_a(t) = \begin{cases} -1 & -T < t < 0 \\ 1 & 0 < t < T \end{cases} \quad (1.41)$$

From this, the acceleration transfer function is

$$|H_a(\omega)|^2 = \frac{k_{\text{eff}}^2}{\omega^2} |H(\omega)|^2 \quad (1.42)$$

which in the low frequency limit  $\omega \ll \Omega$  is

$$|H_a(\omega)|^2 = \frac{16k_{\text{eff}}^2}{\omega^4} \sin^2\left(\frac{\omega T}{2}\right) \quad (1.43)$$

Equivalent definitions for the variance and Allan variance are obtained using this and the acceleration noise spectral density  $S_a(2\pi f)$  as the respective definitions in equation (1.36) and equation (1.37). The transfer function for acceleration noise is shown in Figure 1.19. The gain is largest at low frequencies and approximates a second-order filter at higher frequencies.

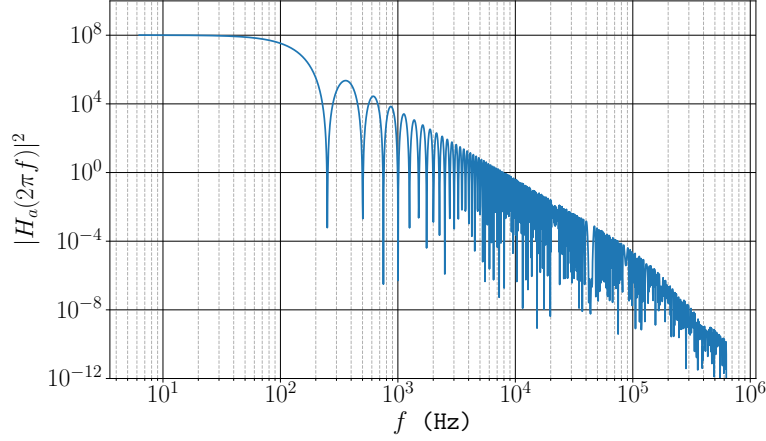


**Figure 1.19:** Acceleration noise transfer function. The parameters used here are the same as those previously defined for Figure 1.17.

### Measuring the Acceleration Noise Power Spectral Density

The interferometer phase is most sensitive to low-frequency vibrations. Acceleration noise at frequencies greater than  $1/2T$  will mostly average out, contributing little to an overall phase. Precise measurements of the interferometer phase rely on reducing the low frequency noise. The vibration of the retro-reflecting mirror is reduced by passively isolating it from its environment. The chamber is mounted on a layer of Sorbothane to dissipate the vibrations from the ground. This isolation is enhanced by a pneumatic suspension system between the optical table and its supporting legs.

A comparison of the acceleration noise spectral density with and without the pneumatic suspension, measured using the accelerometer mounted behind the retro-reflecting mirror, is shown in Figure 1.20. The suspension acts as a low-pass filter and reduces the power within the 10-200 Hz bandwidth, which is aliased into the lower frequency band. For an interferometer pulse separation of  $T = 25$  ms, the vibration phase noise using equation (1.37) is  $\sigma_\Phi = 270$  mrad. Without floating the table, this becomes 7 rad. With the vibration isolation systems currently used, this remains the domi-

nant source of phase noise. More sophisticated methods of damping low-frequency vibrations are required to improve the interferometer's acceleration sensitivity.

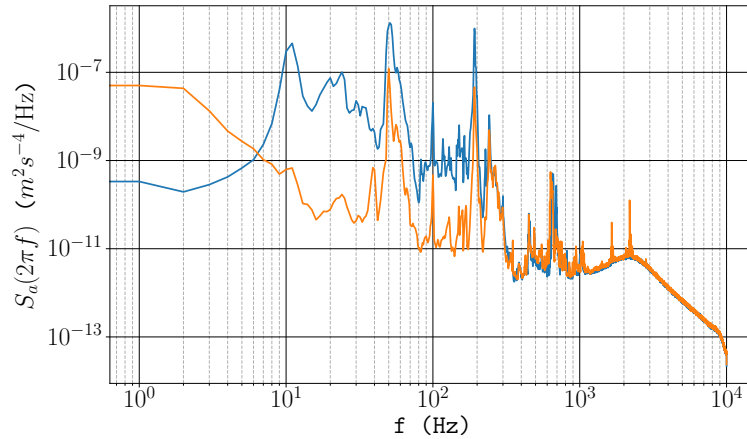


**Figure 1.20:** Acceleration noise power spectral density sampled at a rate of 20 kHz. The orange curve shows the acceleration power spectral density using pneumatic suspension to decrease the coupling of vibrations from the ground to the experiment. For comparison, the blue curve shows the power spectral density without this isolation.

## 1.6 Measuring Accelerations

This section presents

### 1.6.1 Fringe Calibration

Without perfect fringe visibility, the interferometer signal must first be calibrated to infer the phase difference. This is done by varying the phase difference between the two Raman lasers for the middle  $\pi$  pulse. Since the interferometer phase is  $\Delta\Phi = \phi_1 - 2\phi_2 + \phi_3$ , varying  $\phi_2$  induces the largest change in  $\Delta\Phi$ . An interference fringe obtained in this manner is shown in Figure 1.21. In this instance, the contrast is

$C = 0.055$  and the mean probability of detecting in  $|F = 2\rangle$  is  $P_0 = 0.39$ . Fringe fitting described in [8]

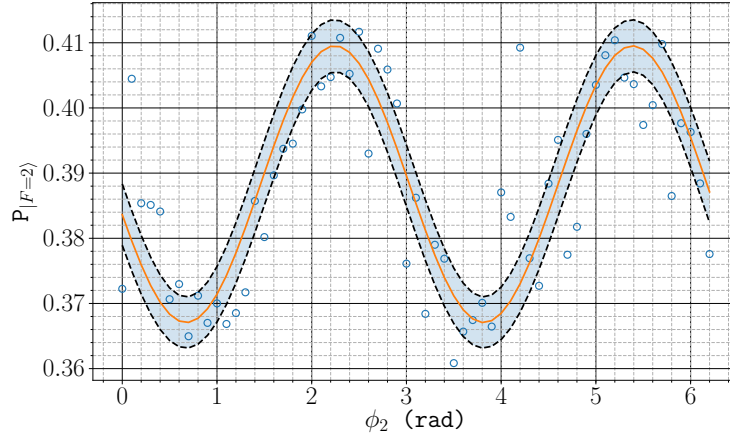


**Figure 1.21:** Interference fringe obtained by varying the phase difference of the two Raman lasers during the middle  $\pi$  pulse for a pulse separation time of  $T = 25$  ms. The orange curve is a non-linear least squares fit to the data, giving a contrast of  $C = 0.055$  and a mean value of  $P_0 = 0.39$ . The shaded region indicates the 95% confidence band.

### 1.6.2 Correcting for Vibration Noise

Vibrations of the retro-reflecting mirror are a significant source of phase noise, which limits the sensitivity of the interferometer to accelerations. This is particularly apparent when the vibration noise induces a phase shift of greater than  $2\pi$  radians. If the interferometer signal spans multiple fringes, it is not possible to accurately determine acceleration from the phase shift.

One method to filter the effects of vibration noise, described in [6], uses the MEMS accelerometer to measure the vibration of the retro-reflecting mirror between the first and last interferometer pulse. After this time, the phase shift due to vibrations is given



by the following convolution

$$\phi_{\text{vib}} = K \int_{-T}^T g_a(t) V(t) dt = K \tilde{V}_{\text{vib}} \quad (1.44)$$

where  $V(t)$  is the voltage measured across the output of the MEMS accelerometer,  $K = 0.793 \text{ m s}^2 \text{ V}^{-1}$  is the scaling factor from voltage to acceleration and  $g_a(t)$  is the acceleration sensitivity function, defined in equation (1.41). The interferometer signal is then fit to the function

$$P_{|F=2\rangle} = P_0 + \frac{C}{2} \sin(\alpha \tilde{V}_{\text{vib}} + \phi_0) \quad (1.45)$$

Common-mode suppression of the vibration phase noise is achieved by estimating the interferometer phase from the residuals of the fit to equation (1.45). If the interferometer phase as estimated from equation (1.7) is denoted  $\phi_{\text{int}}$ , then the fit residuals are  $\phi_{\text{res}} = \phi_{\text{int}} - \phi_{\text{vib}}$ . The correlation of the acceleration measured by the MEMS accelerometer and the interferometer signal is shown in Figure 1.22. The Raman laser phase difference was initially set so that the interferometer signal was at the mid-point of the fringe  $\Delta\phi = \pi/2$  before continuously running the experiment. The vibration noise was increased by removing the pneumatic suspension of the optical table, which helps to passively isolate the experiment from external vibrations that are coupled through the table legs. Without this additional suppression, the vibration noise is large enough to shift the interferometer phase by more than  $2\pi$ , as indicated in Figure 1.22a. When the table is suspended, the vibration noise is small enough that the interferometer signal remains on one side of the fringe.

The suppression of the vibration noise can be seen in the distribution of the estimated acceleration. For the data obtained when the vibrations were more suppressed (Figure 1.22b), histograms of the acceleration measured by the MEMS accelerometer and

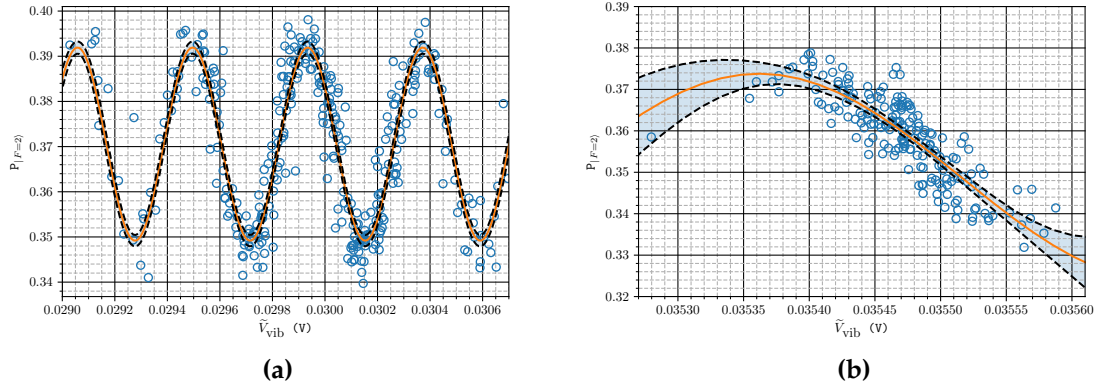


**Figure 1.22:** Correlation between acceleration measured by the MEMS accelerometer and the interferometer signal. **(a)** shows the correlation measured in high vibration environment, when the optical table was not pneumatically suspended. **(b)** shows the reduction in phase noise with this additional vibration isolation.

the interferometer are shown in Figure 1.23. Figure 1.23a compares the distribution of the accelerations measured by the MEMS with that of the interferometer. The

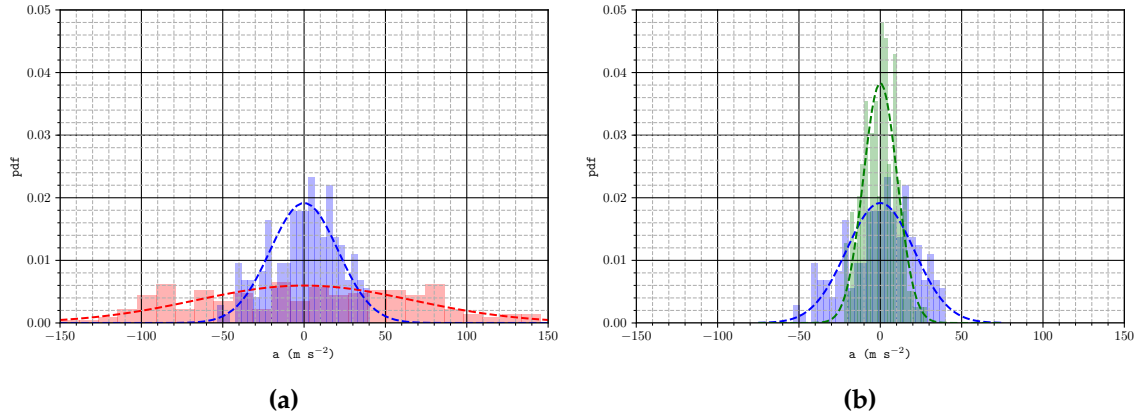


**Figure 1.23:** Histograms of the acceleration noise about the mean value. **(a)** shows the distribution of the acceleration measured by the MEMS accelerometer (red) and the interferometer (blue). **(b)** shows the distribution after filtering the vibration noise from the interferometer signal (green). The dashed lines indicate the fitted normal distributions.

### 1.6.3 Signal Stability

The stability of the interferometer's sensitivity to accelerations can be determined from the Allan deviation. A comparison of the Allan deviation in the presence of high and low vibrations is shown in Figure 1.24. In both instances, the sensitivity to accelerations is improved by correcting for the vibration-induced phase. Under high vibration (Figure 1.24a), the Allan deviation has a minimum value of around  $3 \times 10^{-6} \text{ m s}^{-2}$  after integrating for 35 s. This is a bias instability, i.e. fluctuations in the bias. This value is obtained by subtracting the vibration phase, estimated from the MEMS accelerometer, from the interferometer phase. It is possible that noise in the MEMS accelerometer is contributing to a bias instability.

When the vibration level is reduced, the signal remains stable for a longer period of time. Here, the Allan deviation is proportional to  $\tau^{-1/2}$ , which is characteristic of uncorrelated white phase noise. For longer integration times, the small number of samples introduces a large uncertainty on the Allan deviation in Figure 1.24b. However, for integration times up to 100 s, the sensitivity of the signal is not limited by the same bias instability as in the presence of larger

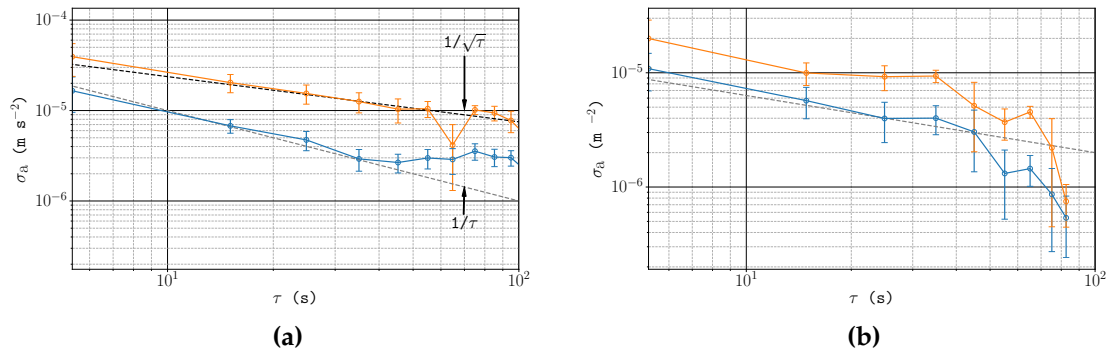


**Figure 1.24:** Allan deviation of the estimated acceleration using the interferometer signal. In each plot the orange curve represents the sensitivity to accelerations without subtracting the vibration induced phase, and the blue curve shows the sensitivity after subtracting this. As in Figure 1.22, (a) shows the sensitivity in a high vibration environment, and (b) shows it after reducing the level of vibration.

# Bibliography

- [1] D.W. Allan. “Statistics of atomic frequency standards”. In: *Proceedings of the IEEE* 54.2 (1966), pp. 221–230. ISSN: 0018-9219. DOI: [10.1109/PROC.1966.4634](https://doi.org/10.1109/PROC.1966.4634).
- [2] Benjamin Canuel. “Étude d’un gyromètre à atomes froids”. PhD thesis. Université Paris Sud - Paris XI, 2007. DOI: [tel-00193288](https://doi.org/10.1018/00193288).
- [3] GJ Dick. “Local oscillator induced instabilities in trapped ion frequency standards”. In: (1987).
- [4] R. W. P. Drever et al. “Laser phase and frequency stabilization using an optical resonator”. In: *Applied Physics B Photophysics and Laser Chemistry* 31.2 (June 1983), pp. 97–105. ISSN: 0721-7269. DOI: [10.1007/BF00702605](https://doi.org/10.1007/BF00702605).
- [5] J Le Gouët, TE Mehlstäubler, and J Kim. “Limits to the sensitivity of a low noise compact atomic gravimeter”. In: *Applied Physics B* (2008), pp. 1–30. arXiv: [arXiv:0801.1270v1](https://arxiv.org/abs/0801.1270v1).
- [6] S Merlet et al. “Operating an atom interferometer beyond its linear range”. In: *Metrologia* 46.1 (Feb. 2009), pp. 87–94. ISSN: 0026-1394. DOI: [10.1088/0026-1394/46/1/011](https://doi.org/10.1088/0026-1394/46/1/011).
- [7] Kathryn Moler et al. “Theoretical Analysis of Velocity-Selective Raman Transitions”. In: *Physical Review A* 45.1 (1992), pp. 342–348.

- 
- [8] A Peters, K Y Chung, and S Chu. "High-precision gravity measurements using atom interferometry". In: *Metrologia* 38.1 (Feb. 2001), pp. 25–61. ISSN: 0026-1394. DOI: [10.1088/0026-1394/38/1/4](https://doi.org/10.1088/0026-1394/38/1/4).
- [9] E Rocco et al. "Fluorescence detection at the atom shot noise limit for atom interferometry". In: *New Journal of Physics* 16.9 (Sept. 2014), p. 093046. ISSN: 1367-2630. DOI: [10.1088/1367-2630/16/9/093046](https://doi.org/10.1088/1367-2630/16/9/093046).
- [10] D. S. Weiss, B. C. Young, and S. Chu. "Precision measurement of  $g$  based on photon recoil using laser-cooled atoms and atomic interferometry". In: *Applied Physics B Lasers and Optics* 59.3 (Sept. 1994), pp. 217–256. ISSN: 0946-2171. DOI: [10.1007/BF01081393](https://doi.org/10.1007/BF01081393).
- [11] P. Welch. "The use of fast Fourier transform for the estimation of power spectra: A method based on time averaging over short, modified periodograms". In: *IEEE Transactions on Audio and Electroacoustics* 15.2 (June 1967), pp. 70–73. ISSN: 0018-9278. DOI: [10.1109/TAU.1967.1161901](https://doi.org/10.1109/TAU.1967.1161901).

